Inorganic Chemistry

Article

pubs.acs.org/IC

Phase Progression of γ-Al_2O_3 Nanoparticles Synthesized in a Solvent-Deficient Environment

Stacey J. Smith,[†,‡] Samrat Amin,[§] Brian F. Woodfield,[‡] Juliana Boerio-Goates,[‡] and Branton J. Campbell*[,†]

[†]Department of Physics and Astronomy and [‡]Department of Chemistry and Biochemistry, Brigham Young University, Provo, Utah 84602, United States

[§]Department of Chemistry and Biochemistry, Arizona State University, Tempe, Arizona 85287, United States

Supporting Information

ABSTRACT: Our simple and uniquely cost-effective solvent-deficient synthetic method produces 3−5 nm Al_2O_3 nanoparticles which show promise as improved industrial catalyst−supports. While catalytic applications are sensitive to the details of the atomic structure, a diffraction analysis of alumina nanoparticles is challenging because of extreme size/microstrain-related peak broadening and the similarity of the diffraction patterns of various transitional Al_2O_3 phases. Here, we employ a combination of X-ray pair-distribution function (PDF) and Rietveld methods, together with solid-state NMR and thermogravimetry/differential thermal analysis-mass spectrometry (TG/DTA-MS), to characterize the alumina phase-progression in our nanoparticles as a function of calcination temperature between 300 and 1200 °C. In the solvent-deficient synthetic environment, a boehmite precursor phase forms which transitions to γ-Al_2O_3 at an extraordinarily low temperature (below 300 °C), but this γ-Al_2O_3 is initially riddled with boehmite-like stacking-fault defects that steadily disappear during calcination in the range from 300 to 950 °C. The healing of these defects accounts for many of the most interesting and widely reported properties of the γ-phase.

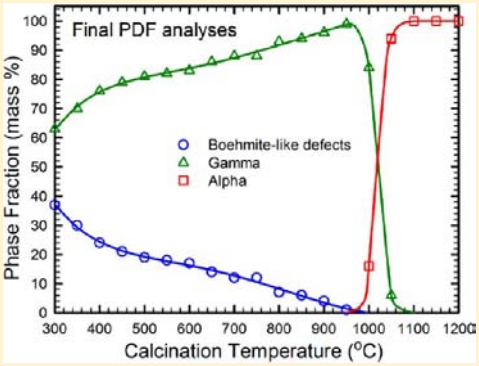

1. INTRODUCTION

The Al_2O_3 (alumina) phase diagram is notoriously complex, having at least 15 reported structural phases (Figure 1a−b).[1−12] The alumina system contains four hydroxide and three oxyhydroxide phases which can, upon heating, transform to one or more of the seven metastable "transitional" Al_2O_3 phases before reaching the thermodynamically stable alpha phase. Adding to the complexity, slight changes in the synthetic conditions, impurities, initial crystallite size, and/or hydrothermal history of the sample alter the phases and transformation temperatures observed.[10,13−17] Hence, a plethora of transition pathways have been reported.[4,9,18−22] Figure 1c shows the most commonly reported sequences.[4,10,14,22]

The phase transformations of alumina have been widely studied because alumina is a technologically and industrially important material with different applications for different phases. For example, the oxyhydroxide boehmite phase and the hydroxides gibbsite and bayerite are used in antacids,[23] as adjuvants in some vaccines,[24] and as the feedstock for the manufacture of many other aluminum compounds including aluminum metal. The hard, high-temperature alpha Al_2O_3 phase (α-Al_2O_3 or corundum) is widely used as a refractory material, as a pigment in paints and sunscreens, and as an abrasive material in sandpapers, cutting tools, and even toothpastes. The metastable transitional Al_2O_3 phases (chi (χ), eta (η), kappa (κ), gamma (γ), delta (δ), theta (θ)) are porous and can be dehydrated and "activated" for use as adsorbents or desiccants. The most widely used of these transitional phases is the γ phase; its porous nature, intrinsically high surface area, and catalytic activity[25] make it a popular catalyst support for a variety of processes including hydrocarbon processing,[26,27] the dehydration of alcohols,[28,29] automotive exhaust gas processing (as in catalytic converters),[30,31] and the Fischer−Tropsch process of converting CO into hydrocarbons for use as fuel.[32−34]

In many of these applications, particularly those of the α and γ phases, alumina nanoparticles are gaining interest and attention. For example, α-Al_2O_3 nanoparticles produce finer grades of sandpapers and allow for thinner layers of paints and sunscreens. Also, γ-Al_2O_3 nanoparticles produce catalyst supports with much more surface area per unit mass than bulk particles, thereby producing catalysts with higher dispersion and efficiency.

We have recently developed a synthetic method[35] capable of producing very small (<5 nm) metal oxide nanoparticles such as Al_2O_3. In this method, solid reagents (a metal salt and a bicarbonate salt) are ground together for 5−30 min, forming a precursor that is then calcined for 1−3 h to yield the metal oxide product. The method is unique in that a traditional solvent is not employed when mixing the reagents, and the resulting "solvent-deficient" synthetic environment seems to

Received: November 27, 2012
Published: April 4, 2013

   dx.doi.org/10.1021/ic302593f | *Inorg. Chem.* 2013, 52, 4411−4423

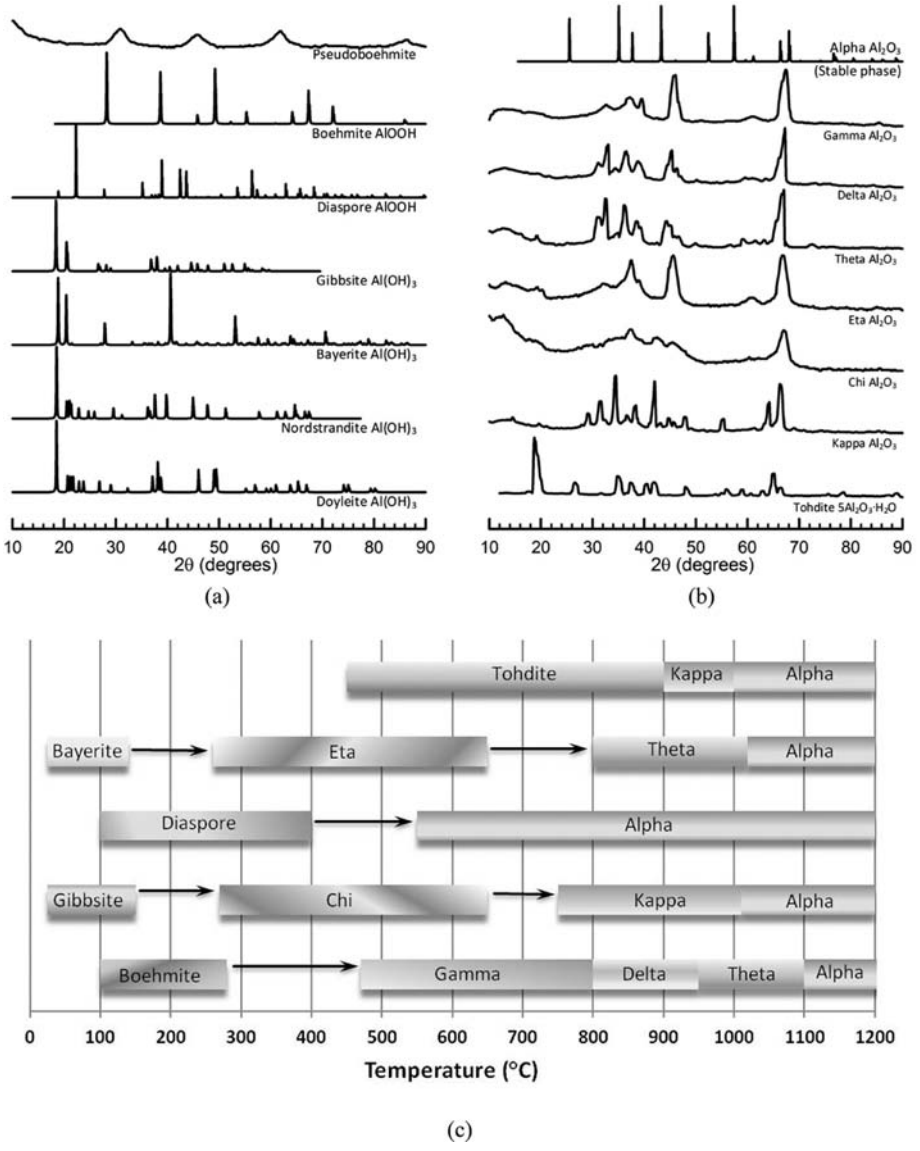

Figure 1. (a, b) XRD patterns of the 15 reported structural phases of the Al_2O_3 system. Part (a) shows the 4 hydroxide and 3 oxyhydroxide phases of the alumina family, namely, pseudoboehmite, boehmite (00-001-0774), diaspore (01-070-2138), gibbsite (00-012-0460), bayerite (00-020-0011), nordstrandite (00-018-0031), and doyleite (00-038-0376) where the numbers in parentheses are the reference numbers of the experimental patterns retrieved from the ICDD database. Part (b) shows the thermodynamically stable alpha phase[69] with the gamma,[10] delta,[10] theta,[10] eta,[10] chi,[10] kappa,[10] and tohdite[9] transitional Al_2O_3 phases (the patterns shown are simulations of those in the given references). (c) Most commonly reported phase transformation pathways of the Al_2O_3 system.[4,10,14,22]

cap particle growth, enabling a single procedure to produce nanoparticles of an unprecedentedly wide range of metal oxides without the use of capping agents.[36] The versatility, simplicity, and cost efficiency of the method make it attractive for a variety of applications, but careful structural characterization is necessary to ensure suitability.

Here, we investigate the structure and properties of Al_2O_3 nanoparticles produced by our solvent-deficient method as a function of synthetic calcination temperature. Transmission electron microscope (TEM) and Brunauer–Emmett–Teller (BET) analyses of the particle size, morphology, surface area, and pore size suggest that this new Al_2O_3 product is a superior candidate for adsorption and catalyst support applications. A combination of X-ray pair-distribution function (PDF) and Rietveld methods, together with solid-state ^{27}Al NMR and thermogravimetry/differential thermal analysis-mass spectrometry (TG/DTA-MS) measurements, demonstrate that the metastable γ-Al_2O_3 phase favored in catalytic applications is achieved at unusually low calcination temperatures, and that the subsequent high-temperature evolution of the local structure explains some of the most interesting and important properties of γ-Al_2O_3, including its tendency to be fine-grained, retain hydrogen, have 5-coordinated Al sites, and display continuous sintering. Comparisons to previous structural analyses are presented alongside the results and interpretation.

2. EXPERIMENTAL SECTION

2.1. Sample Preparation. Alumina nanoparticles were synthesized using a proprietary solvent-deficient method.[35,36] One large batch of the precursor material was prepared by using a mortar and pestle to grind 275.94g of $Al(NO_3)_3{\cdot}9H_2O$ (reagent grade purity, VWR) with 174.45g of NH_4HCO_3 (reagent grade purity, VWR) for 15–20 min, forming a solid precursor in slurry form. The precursor slurry was then dried for 12 h in air at 100 °C using a Thermo

dx.doi.org/10.1021/ic302593f | Inorg. Chem. 2013, 52, 4411–4423

Scientific oven. The dried precursor was split into 23 portions, roughly 8.1 g each. Using the Thermo Scientific oven, one sample was calcined at each 50 °C increment between 100 and 1200 °C by heating it in air at a rate of 5 °C/min to its set temperature and then holding this temperature for 2 h before being allowed to cool to room temperature. Throughout the text of the discussion, each sample will be referred to by its calcination temperature; for example, the "300 °C alumina" refers to the sample in which the alumina precursor was calcined at 300 °C for 2 h. Creating this suite of samples enabled us to study the phases produced through the entire range of synthetic temperatures while still being able to perform ambient temperature diffraction experiments.

In addition to our own suite of Al_2O_3 nanoparticles, we collected PDF data on commercial samples of alumina. This included two samples of boehmite (Sasol and SkySpring Inc.), one sample of α-Al_2O_3 (Alfa Aesar), and four samples of γ-Al_2O_3 including two samples from Sasol (one pure γ-Al_2O_3 sample and one mixture of the γ-, δ-, and θ-phases) and two samples from Alfa Aesar (one labeled as a catalyst support and one simply labeled as having 99.99% purity).

2.2. Experimental Methods. Preliminary powder X-ray diffraction (XRD) data were collected using a PANalytical X'Pert Pro diffractometer with a Cu source and a Ge-111 monochromator that provides a Cu−$K_{\alpha 1}$ (λ = 1.5406 Å) radiation. X-ray PDF data were collected at the 11 ID-B beamline[37] of the Advanced Photon Source (APS) at Argonne National Laboratory using synchrotron radiation of energy 58.2636 keV (λ = 0.2128 Å). For each sample, 10 mg of powder were loaded into a 1.0 mm inner-diameter polyimide (Kapton) capillary, and 2-D images of the diffraction data were collected out to a maximum value of Q = 29.5 $Å^{-1}$ under ambient conditions using a Perkin-Elmer area detector. The Fit2D software package[38] was used to integrate the 2D ring patterns into 1D powder diffraction patterns. The PDFgetX2 software package[39] was used to extract $G(r)$, the experimental PDF,[40] using a maximum value of Q = 24.5 $Å^{-1}$ in the Fourier transform. PDF refinements were performed using the PDFgui program.[41]

Transmission electron microscope (TEM) images of the alumina nanoparticles were recorded using a FEI Philips Technai F20 Analytical STEM operating at 200 kV. Specimens were prepared by dispersing the alumina in ethanol, placing a drop of the very dilute solution on a Formvar/carbon film supported by a 200 mesh Ni grid (Ted-Pella Inc.), and allowing the ethanol to evaporate. Images were recorded in standard high resolution mode.

Thermogravimetric and differential-thermal analyses (TG/DTA) were performed using a Netzsch STA 409PC. Mass spectrometry (MS) measurements were collected in tandem with the TG/DTA measurements using a quadrupole MS unit built in-house.[42] To characterize the water loss and thermal behavior of the Al_2O_3 during calcination between 300 and 1200 °C, three TG/DTA-MS measurements were recorded in which 30−40 mg of the 300 °C alumina were loaded into an alumina crucible and heated at a rate of either 5°/min from 25 to 1100 °C or 3°/min from 25 to 1300 °C under a flowing He atmosphere.

^{27}Al magic angle spinning (MAS) NMR experiments were conducted for the alumina samples calcined at 350, 500, 700, 900 1000, and 1100 °C. The data were collected on a 800 MHz (18.8 T) Varian dual solids/liquids NMR spectrometer operating at a ^{27}Al frequency of 104.16 MHz. The samples were spun in 1.6 mm zirconia rotors at 35 kHz to avoid overlap between the central transition and the first order spinning sidebands. A total of 2048 scans were collected using a 310 ns (π/12) pulse for nonselective excitation along with a 1s recycle delay.[43] All spectra were collected under identical conditions and externally referenced to a 1 M aluminum chloride solution. The ratios of tetrahedral to octahedral coordination environments were quantified by fitting under their respective resonances.

The BET specific surface area and Barrett−Joyner−Halenda (BJH) pore size of each Al_2O_3 sample were determined from N_2 adsorption at 77 K using a Micromeritics TriStar II instrument. For these measurements, roughly 200−300 mg of each sample were degassed at 200 °C for ~24 h to remove adsorbed moisture. The samples were allowed to equilibrate to room temperature prior to being cooled to 77 K for data collection.

3. RESULTS AND DISCUSSION

3.1. Physical Properties. The TEM images in Figure 2a−c illustrate the 3−5 nm diameters of the roughly spherical Al_2O_3

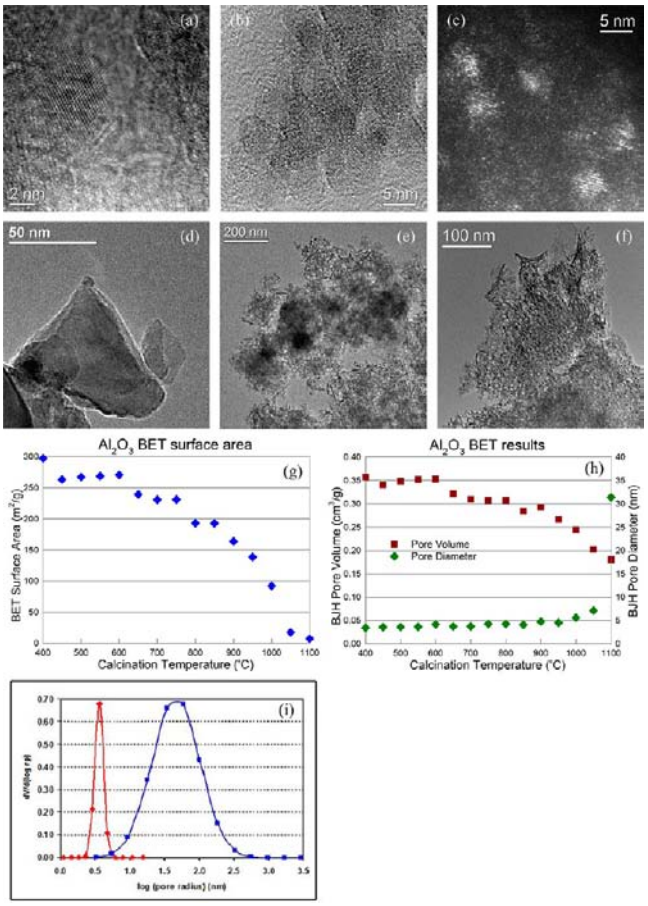

Figure 2. Physical properties characterizations of alumina nanoparticles synthesized via the solvent-deficient method. (a,b,c) High magnification TEM images using mass/thickness contrast (a,b) and dark field contrast (c) to establish the 3−5 nm size of the roughly spherical Al_2O_3 crystallites formed via calcination temperatures between 300 and 950 °C (the images shown are from the 700 °C sample). (d) Image of the large, sintered Al_2O_3 agglomerates produced above 1000 °C (the image shown is from the 1100 °C sample). (e,f) Low magnification images showing the agglomerated nature of both (e) the γ-Al_2O_3 from Alpha Aesar and (f) the Al_2O_3 synthesized using the solvent-deficient method (the 700 °C sample). (g) BET surface area vs calcination temperature. (h) BJH pore volume/diameter vs calcination temperature. (i) Comparison of the BET pore size distributions from commercial (Sasol Pural, blue) and solvent-deficient-method (red) Al_2O_3.

crystallites produced by our new synthetic method at calcination temperatures between 300 and 950 °C. Only these few representative images are shown because the particle size and morphology remain essentially constant in this temperature range. Beyond this temperature, the crystallites sinter to form particles ≥60 nm in size (Figure 2d); but between 300 and 950 °C the crystallites simply aggregate to satisfy the characteristically high surface energies of small nanoparticles,[86] forming the agglomerates seen in Figure 2f. These agglomerates are mesoporous and have high surface

dx.doi.org/10.1021/ic302593f | Inorg. Chem. 2013, 52, 4411−4423

areas (Figure 2g–h), though as the figures show, the surface area and pore volume decrease steadily with increasing temperature as is ubiquitously reported for Al_2O_3. Above roughly 950 °C, a rapid drop in surface area occurs, consistent with the TEM observation that the particles are sintering.

As Figure 2e–f show, commercial samples exhibit the same agglomerated morphology as our Al_2O_3 calcined between 300 and 1000 °C. However, the Al_2O_3 agglomerates formed via the solvent-deficient process have a significantly higher average surface area (Table 1) than most commercial samples that have been calcined at comparable temperatures, which we attribute to the smaller crystallite sizes of the particles within the agglomerates. Because higher surface area allows for greater catalyst dispersion, which correlates to increased efficiency, our alumina is a promising candidate for adsorption and catalyst applications. Specifically, the small pore sizes (Figure 2h) are suitable for the noble metal catalyst used in exhaust gas processing. Additionally, the distribution in pore size (Figure 2i) is roughly half that of commercial materials, which would enable more uniform catalyst sites to form on supports made using our alumina.

Table 1. Surface Area, Pore Size, and Crystallite Size of Al_2O_3 Synthesized via the Solvent-Deficient Method Compared to Commercially Available Products

	BET surface area (m^2/g)	crystallite size (nm)	pore diameter (nm)
BYU alumina	**250**	**3–5**	**1.85**
Davison Mi-286	170–230	22	
Grace Mi-286	300–350	22	5.0
Sasol Puralox	147	30	6.0
Sasol Catalox	191		4.0

These TEM and BET analyses thereby suggest that the physical properties of our Al_2O_3 are as good as or possibly better than those of commercially available materials for adsorption and catalyst support applications. Most of these applications are specific to the γ-Al_2O_3 phase, however, so to truly gauge the industrial viability of our Al_2O_3 we found it necessary to carefully determine the phase progression realized by this new solvent-deficient synthetic method.

3.2. Potential Transition Pathways. A mixture of techniques such as FTIR, TG/DTA, TEM, and NMR are sometimes employed to analyze the structural evolution of Al_2O_3, but most past work has relied primarily on XRD.[20,45−54] As Figure 1a–b illustrate, the unique XRD pattern of each Al_2O_3 phase identifies the structure much like a fingerprint. Accordingly, we collected XRD data for alumina calcined every 50 °C from 100 to 1200 °C to identify the phases produced by the solvent-deficient method as a function of temperature. As Figure 3 shows, at 100 °C, the dried and rinsed precursor strongly resembles boehmite (Figure 3a). By 1100 °C, the alumina clearly matches α-Al_2O_3 (Figure 3c).

With boehmite as the initial phase, there are at least three routes through which the thermodynamically stable α-Al_2O_3 phase can form, according to the excellent review by Wefers and Misra.[10] Poorly crystalline boehmite has been reported to transform first to η-Al_2O_3 and then θ-Al_2O_3 on its way to α-Al_2O_3 (boehmite→η→θ→α), whereas well-crystallized boehmite is thought to transform first to γ-Al_2O_3 and then θ-Al_2O_3 before reaching α-Al_2O_3 (boehmite→γ→θ→α).[10] A third pathway involving a δ-Al_2O_3 phase (boehmite→γ→δ→θ→α) is also commonly reported,[5,55] though no crystal structure has been determined for δ-Al_2O_3. Similarly, χ-Al_2O_3 (an unsolved crystal structure) is sometimes reported to precede or coincide with γ-Al_2O_3,[20,56] though it is more commonly reported in the gibbsite→χ→κ→α transition pathway.[8,19] Still other studies involving extremely small boehmite crystallites found that both the δ and θ phases were completely absent from the boehmite→γ→δ→θ→α pathway, resulting in the greatly simplified boehmite→γ→α pathway in which the γ→α transition occurs at significantly lower temperatures (~1050 °C) than α-Al_2O_3 is typically formed (1100–1200 °C).[18,57] Unfortunately, as Figure 3b shows, in the crucial temperature range between 300 and 1000 °C, the small crystallite sizes (3–5 nm) of our alumina result in extremely broad diffraction peaks which make it difficult or impossible to distinguish between the

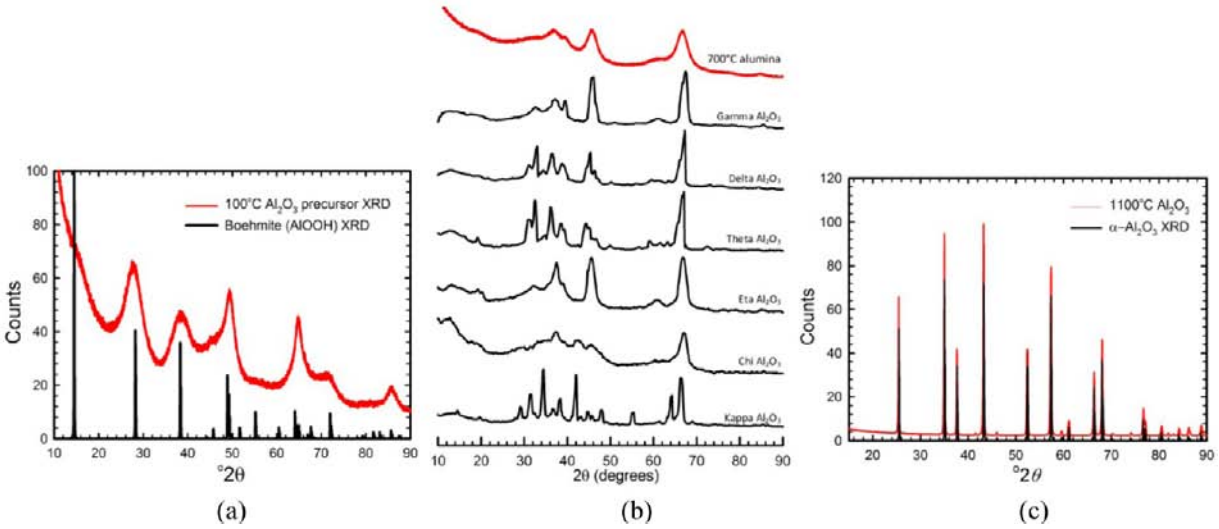

Figure 3. Normalized XRD patterns of (a) the alumina precursor rinsed and dried at 100 °C compared to highly crystalline AlOOH boehmite (ICDD #01-074-2899), (b) the 700 °C Al_2O_3 sample compared to several transitional Al_2O_3 phases (patterns simulated from those given by Wefers and Misra[10]), and (c) the 1100 °C Al_2O_3 sample compared to highly crystalline α-Al_2O_3 (ICDD #04-006-9730).

dx.doi.org/10.1021/ic302593f | Inorg. Chem. 2013, 52, 4411−4423

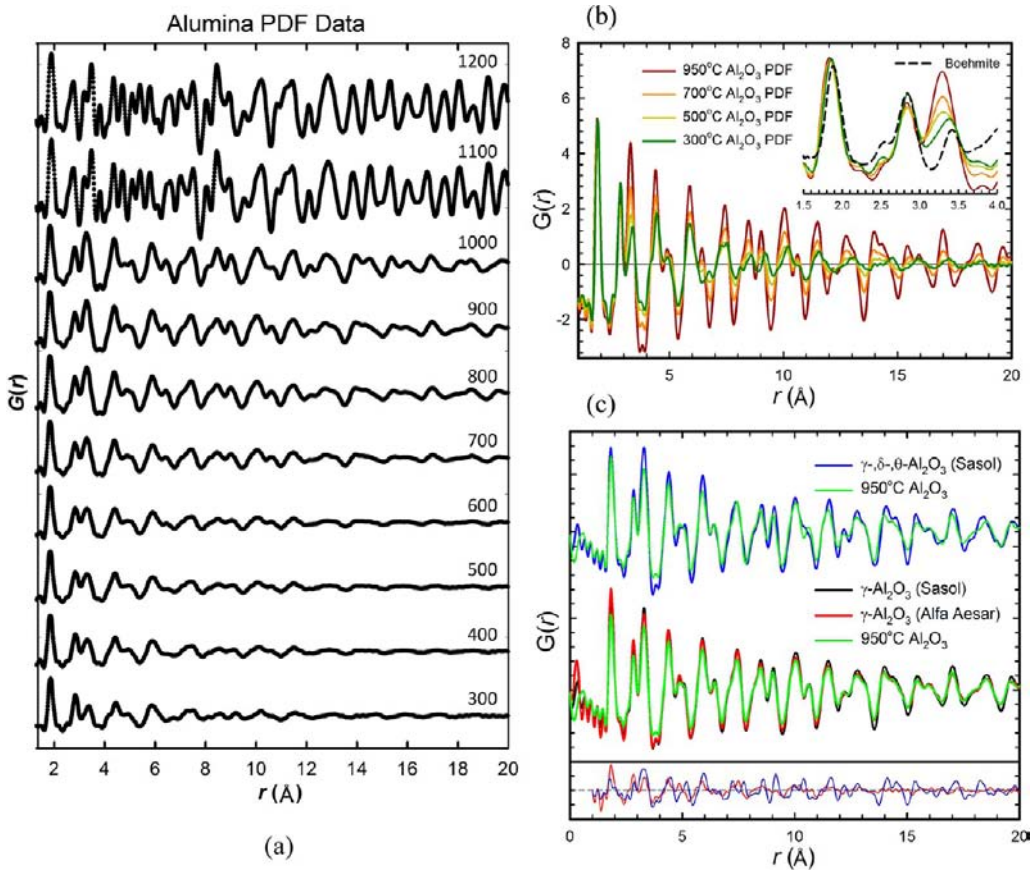

Figure 4. (a) PDF data throughout the full range of calcination temperatures (300−1200 °C). Two phase transitions are visible: (1) an abrupt transition between 1000 and 1100 °C to the α-phase, and (2) a broad transition between 300 and 1000 °C. (b) The evolving ratio of the 2nd and 3rd peaks provides evidence of a broad transition from boehmite to a metastable Al_2O_3 phase between 300 and 1000 °C. (c) The PDF data of this metastable phase (950 °C sample, green) match the commercial γ-Al_2O_3 samples from Sasol (black) and Alfa Aesar (red) significantly better than the $\gamma/\delta/\theta$-Al_2O_3 mixture from Sasol (blue), as the difference curves at the bottom of the graph indicate [blue curve = ($\gamma/\delta/\theta$ mixture) − (950 °C sample)], [red curve = (γ from Alfa Aesar) − (950 °C sample)]. Alumina synthesized via the solvent deficient method thus appears to follow a boehmite→γ→α pathway.

various transitional phases (γ, δ, θ, η, χ, κ) whose diffraction patterns are already very similar.

3.3. Quantitative Phase Comparisons and Evidence of Local Structure in γ-Al_2O_3. To differentiate between the several transitional phases, we attempted Rietveld analyses, which have been reported previously for alumina nanoparticles significantly larger (>20 nm) than our 3−5 nm particles.[17,18,58] However, the extremely broad diffraction peaks of our smaller alumina nanoparticles pushed the Rietveld method beyond its natural limits, resulting in ambiguous and sometimes unphysical refinements. We thus turned to pair distribution function (PDF) analysis,[59,60] a powerful local-structure probe that is being increasingly applied to the study of nanoparticles.[44,58,61−66] Previous PDF studies of the boehmite[58] and γ-alumina[44] phases have provided useful structural information.

In the present work, the PDF method was applied to a series of Al_2O_3 samples that were calcined at temperatures between 300 and 1200 °C (Figure 4a). The data reveal visual evidence for only two transitions. Most recognizably, between 1000 and 1100 °C, a rapid and drastic transformation occurs in the PDF which we know from our preliminary XRD analyses (Figure 3c) to be the transition to the α-Al_2O_3 phase. The second and less obvious transition (highlighted in the inset of Figure 4b) occurs smoothly between 300 and 1000 °C, where we see a steady evolution of the ratio of the second ($r \approx 2.8$ Å) and third ($r \approx 3.4$ Å) peak intensities, suggesting a transition from boehmite to one of the transitional Al_2O_3 phases. Other than this low-r evolution, however, no visually obvious changes occur in the PDF between 300 and 950 °C except that the high-r peaks become more distinct (see Figure 4b), indicating that the coherence length increases with calcination temperature.

As Figure 4c shows, PDF data from the transitional Al_2O_3 phase match the PDF data from commercial γ-Al_2O_3 samples very well. The high-r data in particular resemble γ-Al_2O_3 more strongly than Sasol's $\gamma/\delta/\theta$-Al_2O_3 mixture, as the difference curves best illustrate. Thus, alumina nanoparticles synthesized via the solvent-deficient method initially appear to follow the simplified boehmite→γ→α pathway reported in other studies of small Al_2O_3 particles.[18,57]

[To be certain that only one transitional Al_2O_3 phase is present and that it is indeed γ-Al_2O_3, we fit models of the eta (η),[4] gamma (γ),[11] theta (θ),[4] and kappa (κ)[8] Al_2O_3 phases against PDF data from our 700, 800, and 950 °C samples. For the γ phase, we tested both cubic[4] and tetragonally distorted[11] structures. Because the tetragonal-γ model yielded better fits than the cubic-γ model against data from our 700 °C alumina and from three γ-Al_2O_3 samples from Sasol and Alfa Aesar, we subsequently ignored the cubic model. Hereafter, we imply the tetragonal model whenever we refer to models of γ-Al_2O_3.] (The δ-Al_2O_3 and χ-Al_2O_3 phases could not be tested because

dx.doi.org/10.1021/ic302593f | Inorg. Chem. 2013, 52, 4411−4423

their structures are unknown.) Each of these four structures has roughly the same face-centered cubic (fcc) lattice of oxygen anions, though each is distorted in different ways and to different extents. All contain a mixture of both tetrahedrally and octahedrally coordinated Al as well, though the placement of the Al cations within the oxygen lattice is different for each structure. Given these similarities, it is perhaps not too surprising that all four phases can passably fit the data (Figure 5).

The η and γ phases in particular yielded very comparable fits (Figure 5a–b). Aside from the tetragonal distortion, the tetragonal-γ and cubic-η phases are so similar (differing only in that the Al site occupancies are a little different and that one-third of the Al positions display slightly more displacive disorder in η than in γ) that distinguishing them with different labels seems rather artificial. Hereafter, we will refer to both phases collectively as γ-Al_2O_3.

Despite the similarities, there are also important differences between the fits in Figure 5. The γ model (Figure 5a–b) fits the PDF data significantly better at high-r (above 8 Å) than at low-r, as evidenced by the difference curves at the bottom of each panel. Conversely, the θ and κ structures (Figure 5c–d) fit very well at low-r but noticeably worse than γ at higher r, trends that were also observed with commercial γ-Al_2O_3 samples (see the Supporting Information). The PDF study of γ-Al_2O_3 by Paglia et al.[44] also noted a decrease in fit quality of the γ phase at $r < 8$ Å, which was attributed to the γ-Al_2O_3 local structure being different from the average structure.

To explain these observations, we likewise assert that the local structure of our transitional phase differs from the average structure. Though the average structure is best modeled by the γ structure, we do not believe that the θ and κ phases are accurate representations of the local structure of our transitional phase; instead, we suspect that both structures have sufficiently large unit cells and sufficient displacive freedom to imitate salient features of the actual local structure. Specifically, the monoclinic cell of the θ phase contains five unique atoms, all having two positional degrees of freedom, and the orthorhombic cell of the κ phase contains 9 unique atoms, all on general symmetry positions. This freedom allows the AlO_6 octahedra and AlO_4 tetrahedra to relax/distort into substantially noncubic configurations (see Figure 6). Assuming such distortions occur in a semi-random fashion from one unit cell to the next (i.e., at $r < 8$ Å), they should average out on longer length scales so that the high-r PDF still matches the average structure associated with the γ phase. We thus propose that γ-Al_2O_3 (regardless of the synthetic method) contains randomized, noncubic polyhedral distortions that cause the local structure and average structures to differ.

In agreement with such a semirandom local structure, one first-principles computational study of γ-alumina[67] determined that 40% of the Al atoms reside in nonspinel positions that vary locally within a crystallite. Of these 40%, two-thirds were on c-type Wyckoff sites, and the remainder were on a variety of Wyckoff sites distinct from the usual a, c and d sites to minimize local lattice distortions. Their work suggests that it is more important to have cations in certain Miller planes than on particular Wyckoff sites; hence the formation of a variety of local Al environments across the crystal.

We conclude that the γ-Al_2O_3 label is appropriate for the transitional Al_2O_3 phase that results from our solvent-deficient synthesis, just as it is for numerous commercial materials. But one must appreciate that γ-Al_2O_3, irrespective of synthetic method, has a highly flexible local structure, so that any average structure is merely an idealization of a more complex reality.

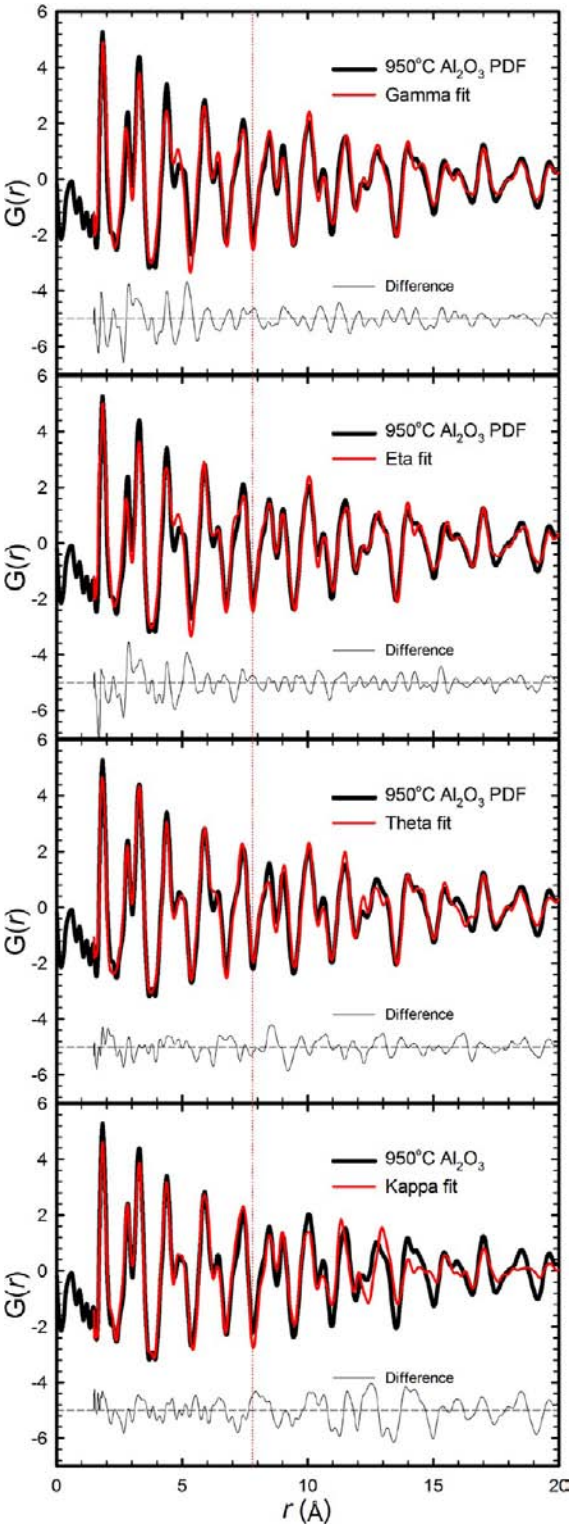

Figure 5. PDF refinements of the 950 °C data using the (a) γ-Al_2O_3, (b) η-Al_2O_3, (c) θ-Al_2O_3, and (d) κ-Al_2O_3 structures. The vertical red line in each graph divides the low-r region ($r \leq 7.8$ Å) where the θ and κ phases fit better from the high-r region ($r \geq 7.8$ Å) where the γ and η phases fit better. Difference curves are shown at the bottom of each graph.

3.4. Temperature Evolution. Having determined that our synthetic method forms the γ phase, it was still necessary to

dx.doi.org/10.1021/ic302593f | Inorg. Chem. 2013, 52, 4411–4423

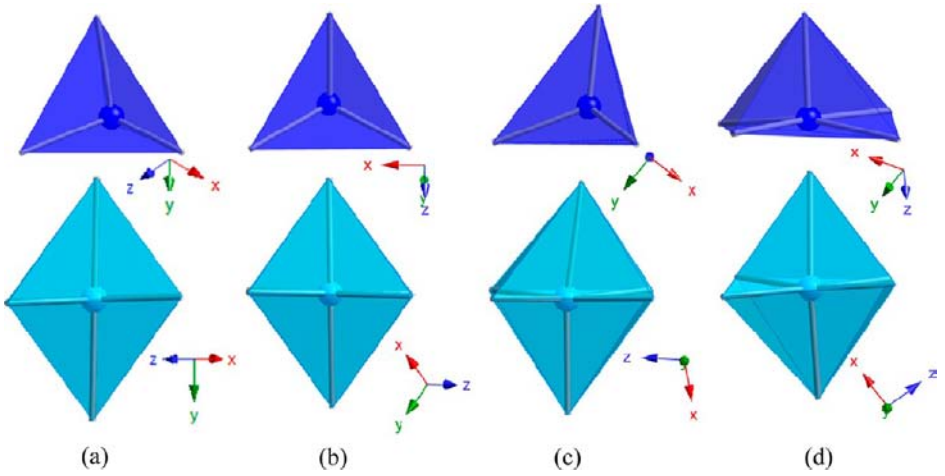

Figure 6. AlO_6 octahedra (light blue) and AlO_4 tetrahedra (dark blue) from the η, γ, θ, and κ (a, b, c, and d, respectively) transitional Al_2O_3 phases.

quantify the phase mixture of the Al_2O_3 product as a function of calcination temperature. Modeling the 300−1200 °C PDF data using a mixture of the boehmite,[68] tetragonal γ-Al_2O_3,[11] and α-Al_2O_3[69] average-structure models (Figure 7), we found that our

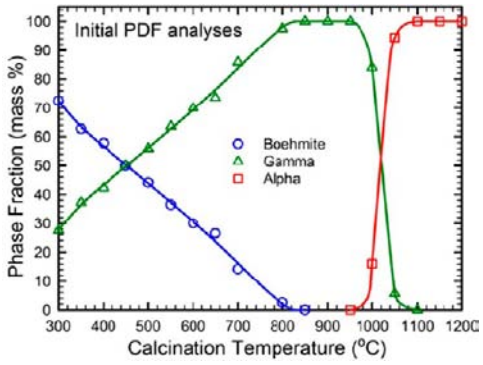

Figure 7. Phase fractions obtained from the initial PDF analyses of a mixture of the boehmite, γ and α phases, which simultaneously fit both low-r and high-r regions with the same model.

γ-Al_2O_3 transforms to α-Al_2O_3 between 1000 and 1100 °C, with the transition being nearly complete by 1050 °C. This is a rather low α-phase transition temperature, but is consistent with the results of previous studies of small Al_2O_3 nanoparticles.[18,57] A direct γ-to-α transition and a corresponding reduction in the transition temperature thus seems to be a general result for small Al_2O_3 particle sizes.

These initial efforts simultaneously fitted the same model to both the low-r and high-r regions of the PDF pattern. Two peculiar features were evident in these initial fits: (1) a significant fraction (~30%) of the γ-Al_2O_3 phase was present at the unusually low temperature of 300 °C, and (2) the boehmite phase did not disappear until roughly 800 °C, which is rather high for an oxyhydroxide. We subsequently collected TG/DTA and MS data in tandem to see if the water loss required by the transition from the boehmite phase (AlOOH) to the γ-Al_2O_3 phase persists up to 800 °C. As Figure 8 shows, water loss indeed continues through 800 °C, but the amount of H_2O evolved cannot justify the rather large boehmite phase fractions (~30%) still present above 600 °C in the initial PDF analyses.

A re-evaluation of the initial PDF fits revealed that the boehmite phase did not model the data well even at the lowest

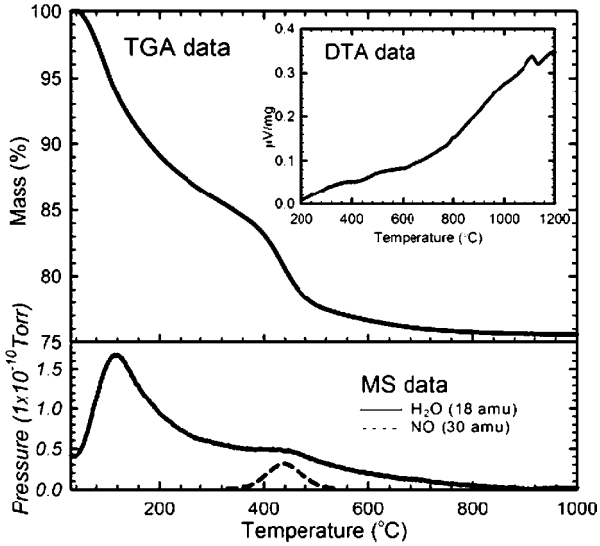

Figure 8. TG/DTA-MS analysis of the 300 °C sample heated at 5 °C/min from 25 to 1200 °C. H_2O evolved below 300 °C is attributed to adsorbed water loss. The small fraction of H_2O evolved between 300 and 800 °C is attributed to the healing of boehmite-like stacking faults in the γ phase. The evolution of NO (375−500 °C) is likely due to the decomposition of residual, adsorbed nitrate species from the synthesis. In the inset, positive DTA values represent exothermic events; the small peak between 1000 and 1100 °C likely corresponds to the $\gamma \rightarrow \alpha$ transition. The constant and steadily increasing exothermic signal below this transition may correspond to the slow healing of boehmite-like features/defects in the alumina with increasing temperature.

calcination temperature of 300 °C (Figure 9a), except for the first two peaks at r = 1.8 and r = 2.8 Å (Figure 9a inset). In contrast, the γ-Al_2O_3 phase alone models the data surprisingly well at 300 °C (Figure 9b) and throughout the entire temperature range up to 950 °C, particularly at high-r when r-series fits are performed (Figure 9d). The γ-Al_2O_3 structure does not yield great low-r fits (Figure 9c) because our average-structure models do not adequately treat the local structure; but the low-r data still match γ-Al_2O_3 far better than boehmite at all calcination temperatures between 300 and 950 °C.

While this is a provocative result, 300 °C is still an atypically low temperature at which to observe the γ-Al_2O_3 phase, particularly as the primary or sole component; reports of which we are aware only show the γ-Al_2O_3 phase appearing in the

dx.doi.org/10.1021/ic302593f | Inorg. Chem. 2013, 52, 4411−4423

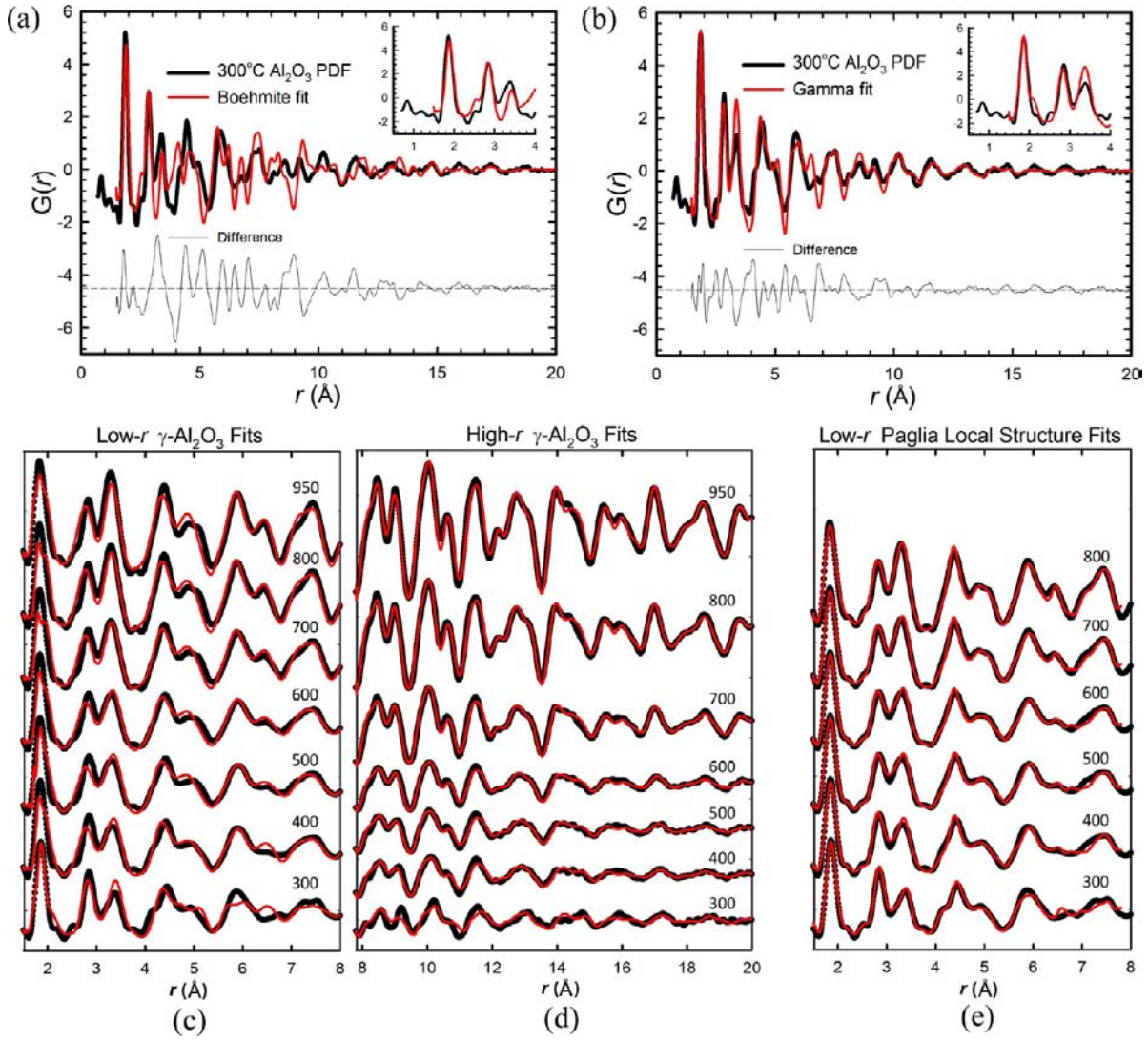

Figure 9. (a,b) PDF data from the 300 °C sample (black) and fits (red) based on the (a) boehmite[68] and (b) γ-Al_2O_3[11] structures. The insets highlight the first few PDF peaks, which the boehmite structure successfully models. (c,d,e) PDF refinements at (c) low-r values ($r \leq 7.8$ Å) and (d) high-r values ($r \geq 7.8$ Å) using only the average γ-Al_2O_3 structure for samples calcined between 300 and 950 °C. (e) PDF refinements at low-r using the local γ-Al_2O_3 structure proposed by Paglia et al.[44]

range 450−650 °C (Figure 1c).[4,10,22,70] To illuminate the matter, we performed ^{27}Al MAS NMR analyses on several representative samples (Figure 10). ^{27}Al MAS NMR is an effective tool for distinguishing the γ-Al_2O_3 phase from the boehmite and α-Al_2O_3 phases because Al coordination is exclusively octahedral in both the α-Al_2O_3 and boehmite phases[71] whereas it is roughly 70% (±2%) octahedral and ~30% tetrahedral in the γ-Al_2O_3 phase.[11,54] The Al coordination ratios quantified from the data in Figure 10 are given in Table 2 (see the Supporting Information for the fits used in the integrations). Though there is a slight conversion of octahedral to tetrahedral coordination between 300 and 700 °C, the Al coordination is already predominantly γ-like at 300 °C and remains so through 1000 °C, thereby supporting the conclusion that γ-Al_2O_3 is the primary phase throughout this temperature range.

The NMR data in Figure 10 and Table 2 also reveal a significant amount (>5%) of 5-coordinated Al sites in the γ-Al_2O_3, which is in agreement with several other high resolution ^{27}Al MAS NMR studies of γ-Al_2O_3.[53,72−78] The fraction of these sites increases slightly from 300 to 700 °C and then decreases substantially between 900 and 1000 °C (Table 2), as was observed in at least one of these studies.[77] Several groups have suggested that these 5-coordinated sites are surface sites,[53,72,73] though others have reasoned that they may exist in within the crystal.[79]

3.5. Temperature Evolution Revisited. Together, the ^{27}Al MAS NMR and PDF data indicate that γ-Al_2O_3 is the dominant phase in our samples calcined at temperatures between 300 and 1000 °C. Though the γ-Al_2O_3 phase fits the high-r data well at all temperatures (Figure 9d), the low-r fit quality steadily decreases with decreasing temperature (Figure 9c) because of local-structure effects. We explained previously that the θ and κ models were able to artificially fit the low-r region of the high-temperature data (700−950 °C) somewhat better because of their greater displacive freedoms. But we now point out that even lowering the symmetries of the γ, θ, or κ models to $P1$ in their respective unit cells fails to accommodate the most distinct feature in the low-r temperature series; no matter how much displacive freedom is allowed, none of the

dx.doi.org/10.1021/ic302593f | Inorg. Chem. 2013, 52, 4411−4423

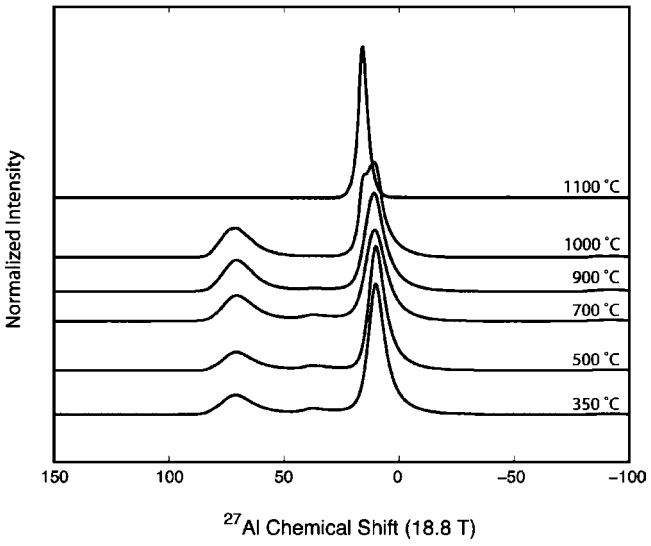

Figure 10. ^{27}Al MAS NMR data for the 350, 500, 700, 900, 1000, and 1100 °C samples showing the ratios of tetrahedral, pentahedral, and octahedral Al^{3+} (at shifts of roughly −70, −35, and −10 ppm, respectively) in each sample.

Table 2. Quantification of the 4-, 5-, and 6-Coordinated Al Sites in Alumina Samples Calcined at 350, 500, 700, 900, 1000, and 1100°C from ^{27}Al MAS-NMR Data[a]

	4-coord. Al	5-coord. Al	6-coord. Al
boehmite	**0**	**0**	**100%**
γ-Al_2O_3	**30%**	**0**	**70 (±2)%**
α-Al_2O_3	**0**	**0**	**100%**
350 °C	19%	5.4%	75%
500 °C	20%	5.2%	75%
700 °C	27%	6.4%	67%
900 °C	31%	2.7%	66%
1000 °C	30%	2.0%	68%
1100 °C	0	0	100%

[a]The ratios of Al coordination typical to the boehmite, γ, and α alumina phases are given for reference in bold at the top of the table.

transitional alumina structures can imitate the steady low-temperature evolution of the ratio of the second and third peak intensities (Figure 4b), which we will call $R_{2/3}$.

Recall that the one helpful feature of the boehmite model was that it nicely fit these low-r peaks at low temperatures (Figure 9a), which leads us to more closely examine their origins in the structure. For both the boehmite and γ-Al_2O_3 phases, we find that the first peak in the PDF ($r \approx 1.8$ Å) represents nearest-neighbor Al−O distances, the second peak ($r \approx 2.8$ Å) includes both nearest-neighbor O−O and Al−Al distances, and the third peak ($r \approx 3.4$ Å) primarily represents third-nearest-neighbor Al−O distances. However, the layered boehmite (AlOOH) structure shown in Figure 11a illustrates that the O−O separations between oxygen atoms in adjacent layers would provide an additional contribution to the second peak in boehmite, making it somewhat higher for boehmite (Figure 4b) than for γ. And in the γ phase, the inclusion of several longer Al−Al distances causes the area of the third peak to be significantly larger than for boehmite.

Figure 12 tracks the $R_{2/3}$ ratio as a function of calcination temperature, where it clearly shifts from a more boehmite-like

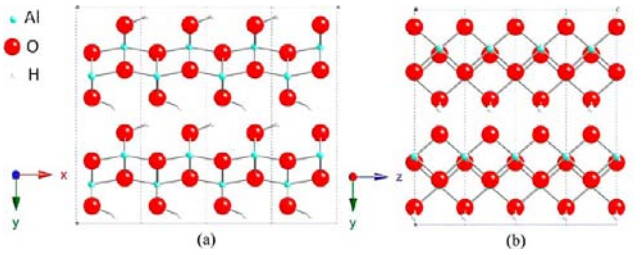

Figure 11. Views of the boehmite structure highlighting (a) the OH groups between the oxide layers and (b) the z-axis misalignment between the oxygen columns on opposite sides of a hydroxide layer, which must be resolved (by a $z/2$ translation) to form the γ phase. Otherwise, stacking faults will be present in the oxygen sublattice, with residual OH groups and awkwardly coordinated Al bridging the gap.

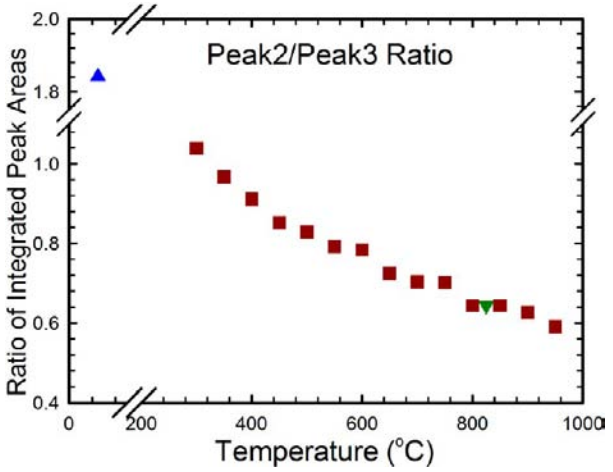

Figure 12. Ratio of the 2nd/3rd PDF peak intensities (red squares) between 300 and 1000 °C which evolves from a boehmite-like value (blue triangles) to a γ-like value (green triangles), providing evidence for a boehmite-like local structure within γ-Al_2O_3 that disappears with increasing temperature.

ratio at 300 °C to a very γ-like ratio, achieving nearly complete conversion to a γ-like ratio by 800 °C. Because the existence of an extended boehmite structure is convincingly refuted by the high-r PDF analyses in Figure 9d and the NMR data in Table 2, we instead hypothesize that a boehmite-like local structure initially exists within the γ-Al_2O_3 calcined at 300 °C, but then slowly evolves/disappears as the material is subsequently heated to higher temperatures. Conveniently, Paglia et al. has suggested just such a local structure model to account for the low-r misfits observed in their PDF study of highly crystalline γ-Al_2O_3 prepared at 600 °C.[44]

We observe that a boehmite-to-γ transition can be effected by (1) removing all of the OH groups between the boehmite layers in Figure 11a, (2) translating every other boehmite layer by $z/2$ in Figure 11b, and (3) shifting 30% of the octahedral Al atoms to tetrahedral sites. In the local-structure model of Paglia et al.,[44] the translation step is left out leaving stacking-fault defects in an otherwise fcc oxygen sublattice, which are then bridged by awkwardly coordinated Al atoms in the gap (see the reference for a visual representation). We therefore reason that the low-r evolution in our PDF data as the calcination temperature is raised from 300 to 800 °C represents the healing of such boehmite-like stacking-fault defects.

Using the model of Paglia et al.,[44] we fit the low-r PDF data (1.5 Å $\leq r \leq$ 7.8 Å) from our Al_2O_3 nanoparticles prepared

dx.doi.org/10.1021/ic302593f | Inorg. Chem. 2013, 52, 4411−4423

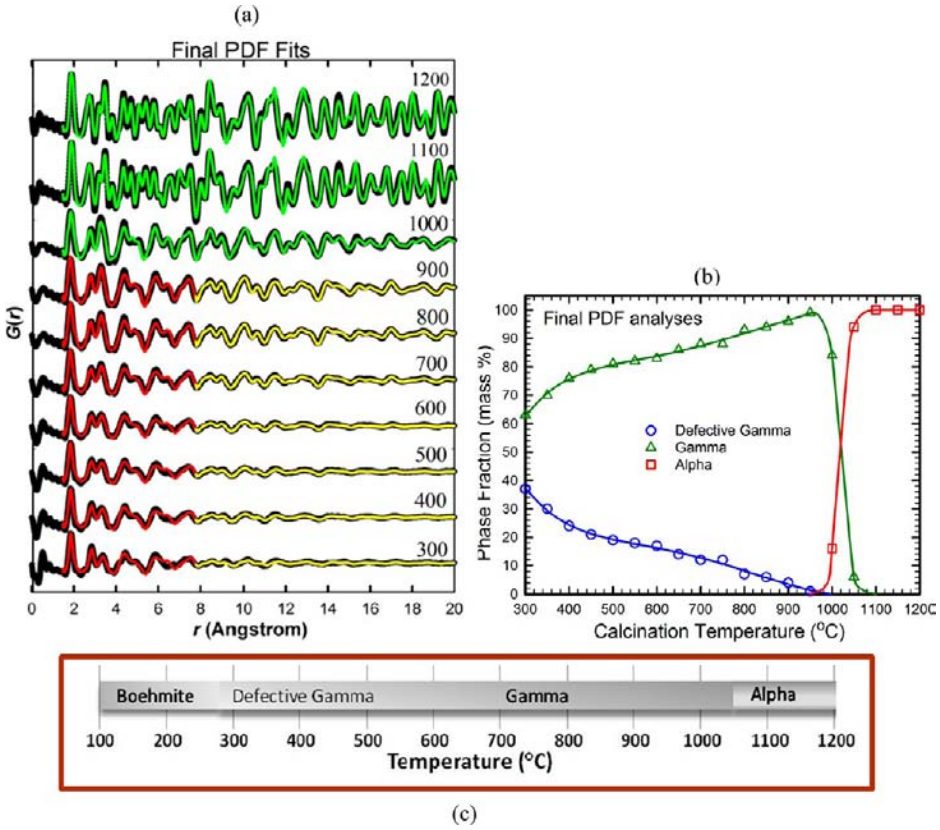

Figure 13. (a) Final PDF fits. Between 300 and 950 °C, the high-r data were fit using only the γ-Al_2O_3 structure (yellow), and the low-r data were fit with a mixture of γ-Al_2O_3 and boehmite (red) to model the effects of a continuously variable boehmite-like defect concentration. Data between 1000 and 1100 °C were fit using a mixture of γ-Al_2O_3 and α-Al_2O_3 (green). (b) Relative concentrations of defective γ-Al_2O_3 (blue), nondefective γ-Al_2O_3 (green), and α-Al_2O_3 (red) as a function of calcination temperature. (c) Phase progression of the Al_2O_3 nanoparticles synthesized via the solvent-deficient method.

between 300 and 950 °C. The results are impressive throughout the entire temperature range, as Figure 9e shows. However, we strongly caution the reader not to interpret this result too literally. The key to fitting the low-r local-structure data is a combination of displacive flexibility and a model that accommodates the right kind of interatomic displacements. The Paglia model has both, but is still ultimately a relatively small supercell with a very limited range of local environments that are so distorted in both our low and high-temperature fits as to be grossly unphysical. Additionally, because the model has a static defect concentration, it cannot accommodate the elimination of the defects at high temperatures; instead, the atomic positions take up the slack by becoming increasingly inappropriate.

While the local structure model of Paglia et al. is conceptually very helpful, a properly refinable boehmite-like local structure model that evolves realistically with temperature would require a big-box modeling approach in which a variety of boehmite-like planar defects are incorporated into the average γ-Al_2O_3 structure and minimized against both energy and experimental PDF data. Such a study is left to future endeavors. To quantify the local defect population as a function of temperature, we took a simpler approach of refining a mixture of the boehmite and γ-Al_2O_3 average structures at low-r only from 300 to 950 °C, where local-structure effects are relevant (Figure 13a). The refined boehmite phase fraction then provides a rough measure of the defect concentration (Figure 13b). At each temperature, we also performed a single-phase refinement of the γ-Al_2O_3 average structure at high-r only (Figure 13a). The fits were of very high quality (see Table S1 in the Supporting Information for fit details) and revealed a surprisingly high (40%) defect concentration at 300 °C, which steadily decreases with increasing temperature. The defects were nearly gone by 800 °C and completely gone by 950 °C, just prior to the transformation to α-Al_2O_3.

4. CONCLUSIONS

The γ-Al_2O_3 produced using our solvent-deficient synthetic method are a promising candidate for catalyst support and adsorption applications because of the small 3−5 nm particle size, high surface area, and mesoporous nature of the agglomerates. X-ray PDF, ^{27}Al MAS NMR, and TG/DTA analyses show that a boehmite precursor phase initially forms but transforms to γ-Al_2O_3 upon calcination to 300 °C, a much lower temperature than previously considered possible. This γ phase is initially riddled with boehmite-like defect planes either within the particles or at interparticle interfaces, which heal as temperature increases, as manifested by the evolution of the $R_{2/3}$ peak ratio in the low-r PDF data. At 1050 °C, the γ-Al_2O_3 phase abruptly and directly transforms to α-Al_2O_3. This simplified boehmite→γ→α pathway and low γ→α transformation temperature appear to be a general result for very small alumina nanoparticles.

We hypothesize that the layered-oxyhydroxide structure of our boehmite precursor has an abnormally low water/OH content because of the solvent-deficient environment in which

dx.doi.org/10.1021/ic302593f | Inorg. Chem. 2013, 52, 4411−4423

it was formed, as we have found with other oxyhydroxide materials formed via this method.[80] Such a precursor would already have a substantial number of oxide bridges across the incomplete hydroxide layers, which explains why the γ phase is able to form as such a low temperature. Of course, there is also a general tendency toward lower transformation temperatures in smaller particle sizes;[15,17,52,81,82] but the formation of the γ phase below 300 °C is extraordinary and requires a different mechanism.

At 300 °C, the γ phase still has a substantial concentration of boehmite-like stacking-fault defects. Instead of having a distinct mobility threshold temperature, these defects heal slowly over a wide range of annealing temperatures from 300 to 800 °C, explaining the impressive H_2O sorbent abilities of γ-Al_2O_3 and the high-temperature H retention often reported in the literature[83−85] and also seen in our own TG/DTA-MS analyses (Figure 8). It is likely that OH groups, absorbed/adsorbed H_2O, and bridging Al atoms stabilize these gaps in the structure and inhibit the locally diffusive healing process. A wide variety of local configurations with different stabilization energies then results in a very broad transformation.

The awkward configurations of the bridging Al atoms that stabilize the stacking faults could explain the significant fraction of pentacoordinated Al sites observed exclusively in the γ phase of Al_2O_3. Indeed, some of the bridging Al in the Paglia et al. local structure must be pentacoordinated; and the healing of the stacking-fault defects would nicely explain the observed decrease in the concentration of pentacoordinated sites with increasing temperature (Table 2).

A high-concentration of stacking-fault defects should also reduce the crystallinity (i.e., X-ray coherence length) of our nanoparticles. The healing of these defects provide an explanation for the substantial increase in crystallinity apparent in the PDF data between 300 and 1000 °C (Figure 4a) despite the fact that no substantial increase in average crystallite size is detected in TEM images. We suspect that the "amorphous" phase often reported between the boehmite and γ phases in the 300−500 °C range (Figure 1c) is actually γ-Al_2O_3 with a high concentration of boehmite-like stacking-fault defects.

Because several ^{27}Al NMR studies have reported pentacoordinated Al to be on the surface,[53,73] the boehmite-like defect planes (adsorbed H_2O, pentacoordinated Al) may be preferentially located at interparticle interfaces within the larger agglomerates seen in TEM images (Figure 2a−f). The healing of surface defects, resulting in mild sintering, explains the steady decrease in BET surface area with increasing temperature (Figure 2g) that is ubiquitously observed for γ-Al_2O_3. The resulting relaxation of the structure as the stacking faults heal also explains the steady exothermic signal in the DTA measurements in the range between 300 and 1000 °C (inset of Figure 8). In short, an evolving boehmite-like defect structure within γ-Al_2O_3 can potentially account for many of its most intriguing and useful properties. And because many of these properties are common to γ-Al_2O_3 materials formed by other synthetic processes, the evolving boehmite-like local structure that we have identified may be generally relevant.

■ ASSOCIATED CONTENT

Supporting Information

(1) PDF data from two commercial γ-Al_2O_3 samples are fit using the γ, η, θ, and κ phases, demonstrating the presence of a comparable γ-like local structure in samples of varied origin; (2) ^{27}Al MAS NMR data for the 350, 500, 700, 900, 1000, and 1100 °C samples, shown together with the fitted curves used to integrate the peak areas and thereby quantify the 4, 5, and 6-coordinated Al in each sample, and (3) tables of the final PDF fit parameters. This material is available free of charge via the Internet at http://pubs.acs.org.

■ AUTHOR INFORMATION

Corresponding Author

*E-mail: branton_campbell@byu.edu.

Notes

The authors declare no competing financial interest.

■ ACKNOWLEDGMENTS

We thank Katharine Page and Hyungjeong Kim for assisting with the collection of preliminary X-ray PDF data. Use of the Advanced Photon Source at Argonne National Laboratory was supported by the U.S. Department of Energy, Office of Science, Office of Basic Energy Sciences, under Contract No. DE-AC02-06CH11357. Other funding for this work was provided by the U.S. Department of Energy under Grant DE-FG02-05ER15666. The laboratory diffractometer was purchased using funds from the National Science Foundation under Grant CHE-0959862.

■ REFERENCES

(1) Saalfeld, H. *Naturwissenschaften* **1961**, *48*, 24.
(2) Bezjak, A.; Jelenic, I. *Symp. Bauxites, Oxydes Hydroxydes Alum., [C. R.]* **1964**, *1*, 105−112.
(3) Ewing, F. J. *J. Chem. Phys.* **1935**, *3*, 203−207.
(4) Zhou, R. S.; Snyder, R. L. *Acta Crystallogr., Sect. B: Struct. Sci.* **1991**, *B47* (5), 617−630.
(5) Rooksby, H. P.; Rooymans, C. J. M. *Clay Miner. Bull.* **1961**, *4*, 234−238.
(6) Mekasuwandumrong, O.; Kominami, H.; Praserthdam, P.; Inoue, M. *J. Am. Ceram. Soc.* **2004**, *87* (8), 1543−1549.
(7) Saalfeld, H.; Wedde, M. *Z. Krsitallogr.* **1974**, *139* (1−2), 129−135.
(8) Ollivier, B.; Retoux, R.; Lacorre, P.; Massiot, D.; Ferey, G. *J. Mater. Chem.* **1997**, *7* (6), 1049−1056.
(9) Yamaguchi, G.; Yanagida, H.; Ono, S. *Bull. Chem. Soc. Jpn.* **1964**, *37* (10), 1555−1557.
(10) Wefers, K. M., Chanakya Oxides and Hydroxides of Aluminum. Tech. Paper. - Alcoa Res. Lab. **1987**, Vol. *19*.
(11) Paglia, G.; Buckley, C. E.; Rohl, A. L.; Hunter, B. A.; Hart, R. D.; Hanna, J. V.; Byrne, L. T. *Phys. Rev. B: Condens. Matter Mater. Phys.* **2003**, *68* (14), 144110/1−144110/11.
(12) Yamaguchi, G.; Yanagida, H.; Ono, S. *Bull. Chem. Soc. Jpn.* **1964**, *37* (5), 752−754.
(13) Du, X.; Wang, Y.; Su, X.; Li, J. *Powder Technol.* **2009**, *192* (1), 40−46.
(14) Levin, I.; Brandon, D. *J. Am. Ceram. Soc.* **1998**, *81* (8), 1995−2012.
(15) Tsukada, T.; Segawa, H.; Yasumori, A.; Okada, K. *J. Mater. Chem.* **1999**, *9* (2), 549−553.
(16) Sato, T.; Sue, K.; Akiyama, Y.; Shibata, K.; Kawasaki, S.-i.; Tanaka, S.; Saitoh, K.; Kawai-Nakamura, A.; Aida, K.; Hiaki, T. *Chem. Lett.* **2008**, *37* (3), 242−243.
(17) Bokhimi, X.; Toledo-Antonio, J. A.; Guzman-Castillo, M. L.; Hernandez-Beltran, F. *J. Solid State Chem.* **2001**, *159* (1), 32−40.
(18) Cava, S.; Tebcherani, S. M.; Souza, I. A.; Pianaro, S. A.; Paskocimas, C. A.; Longo, E.; Varela, J. A. *Mater. Chem. Phys.* **2007**, *103* (2−3), 394−399.
(19) Brindley, I. G. W.; Choe, J. O. *Am. Mineral.* **1961**, *46*, 771−785.
(20) Kim, Y. M.; Lee, S.; Kim, Y. S.; Oh, S. H.; Kim, Y. J.; Lee, J. Y. *Scr. Mater.* **2008**, *59* (9), 1022−1025.

(21) Lippens, B. C.; de Boer, J. H. *Acta Crystallogr.* **1964**, *17* (10), 1312−1321.
(22) Digne, M.; Sautet, P.; Raybaud, P.; Toulhoat, H.; Artacho, E. *J. Phys. Chem. B* **2002**, *106* (20), 5155−5162.
(23) Galbraith, A. B., S; Manias, E.; Hunt, B.; Richards, A. *Fundamentals of pharmacology: a text for nurses and health professionals*; Pearson: Harlow, England, 1999.
(24) Petrovsky, N. A., J. C. *Immunol. Cell Biol.* **2004**, *82* (5), 488−496.
(25) Cai, S.-H.; Rashkeev, S. N.; Pantelides, S. T.; Sohlberg, K. *Phys. Rev. B: Condens. Matter Mater. Phys.* **2003**, *67* (22), 224104/1−224104/10.
(26) Ivey, M. M.; Allen, H. C.; Avoyan, A.; Martin, K. A.; Hemminger, J. C. *J. Am. Chem. Soc.* **1998**, *120* (42), 10980−10981.
(27) Trombetta, M.; Busca, G.; Rossini, S.; Piccoli, V.; Cornaro, U.; Guercio, A.; Catani, R.; Willey, R. J. *J. Catal.* **1998**, *179* (2), 581−596.
(28) Cai, S.; Sohlberg, K. *J. Mol. Catal. A: Chem.* **2003**, *193* (1−2), 157−164.
(29) Shi, B.; Davis, B. H. *J. Catal.* **1995**, *157* (2), 359−367.
(30) Taylor, K. C. *Catal, Rev. - Sci. Eng.* **1993**, *35* (4), 457−481.
(31) McCabe, R. W.; Usmen, R. K.; Ober, K.; Gandhi, H. S. *J. Catal.* **1995**, *151* (2), 385−393.
(32) Chu, W.; Chernavskii, P. A.; Gengembre, L.; Pankina, G. A.; Fongarland, P.; Khodakov, A. Y. *J. Catal.* **2007**, *252* (2), 215−230.
(33) Itkulova, S. S.; Zakumbaeva, G. D.; Arzumanova, R. S.; Ovchinnikov, V. A. *Stud. Surf. Sci. Catal.* **2007**, *163*, 75−85.
(34) van Steen, E.; Viljoen, E. L.; van de Loosdrecht, J.; Claeys, M. *Appl. Catal., A* **2008**, *335* (1), 56−63.
(35) Woodfield, B. F.; Liu, S.; Boerio-Goates, J.; Liu, Q. Preparation of Uniform Nanoparticles of Ultra-High Purity Metal Oxides, Mixed Metal Oxides, Metals, and Metal Alloys. U.S. Patent No. 8,211,388, 2012.
(36) Smith, S. J.; Liu, S.; Liu, Q.; Olsen, R. E.; Rytting, M.; Selck, D. A.; Simmons, C. L.; Boerio-Goates, J.; Woodfield, B. F. *Microporous Mesoporous Mater.* **2012**, submitted for publication.
(37) Rutt, U.; Beno, M. A.; Strempfer, J.; Jennings, G.; Kurtz, C.; Montano, P. A. *Nucl. Instrum. Methods Phys. Res., Sect. A* **2001**, *467*−*468* (Pt. 2), 1026−1029.
(38) Hammersley, A. P. *Fit2D*, V. 9.129 Reference Manual V. 3.1; European Synchrotron Radiation Facility: Grenoble, France.
(39) Qiu, X.; Thompson, J. W.; Billinge, S. J. L. *J. Appl. Crystallogr.* **2004**, *37* (4), 678.
(40) Egami, T. B., S. J. L. *Underneath the Bragg Peaks: Structural Analysis of Complex Materials*, 1st ed.; Pergamon: Kidlington, Oxford, U.K., 2003; Vol. 7, p 404.
(41) Farrow, C. L.; Juhas, P.; Liu, J. W.; Bryndin, D.; Bozin, E. S.; Bloch, J.; Proffen, T.; Billinge, S. J. L. *J. Phys.: Condens. Matter* **2007**, *19* (33), 335219/1−335219/7.
(42) Selck, D. A.; Woodfield, B. F.; Boerio-Goates, J.; Austin, D. E. *Rapid Commun. Mass Spectrom.* **2012**, *26* (1), 78−82.
(43) Massiot, D.; Bessada, C.; Coutures, J. P.; Taulelle, F. *J. Magn. Reson.* **1990**, *90*, 231−242.
(44) Paglia, G.; Bozin, E. S.; Billinge, S. J. L. *Chem. Mater.* **2006**, *18* (14), 3242−3248.
(45) Balint, I.; Miyazaki, A. *Microporous Mesoporous Mater.* **2009**, *122* (1−3), 216−222.
(46) Kim, Y.; Kim, H. S.; Martin, S. W. *Electrochim. Acta* **2006**, *52* (3), 1316−1322.
(47) Ram, S. R., S. *Indian J. Phys.* **2001**, *75A* (4), 437−441.
(48) Azar, M.; Palmero, P.; Lombardi, M.; Garnier, V.; Montanaro, L.; Fantozzi, G.; Chevalier, J. *J. Eur. Ceram. Soc.* **2008**, *28* (6), 1121−1128.
(49) Mekasuwandumrong, O.; Praserthdam, P.; Inoue, M.; Pavarajarn, V.; Tanakulrungsank, W. *J. Mater. Sci.* **2004**, *39* (7), 2417−2421.
(50) Tartaj, P.; Tartaj, J. *Chem. Mater.* **2002**, *14* (2), 536−541.
(51) Roman, R.; Hernandez, T.; Gonzalez, M. *Bol. Soc. Esp. Ceram. Vidrio* **2008**, *47* (6), 311−318.
(52) Kim, H. J.; Kim, T. G.; Kim, J. J.; Park, S. S.; Hong, S. S.; Lee, G. D. *J. Phys. Chem. Solids* **2007**, *69* (5−6), 1521−1524.
(53) Kwak, J. H.; Hu, J.; Lukaski, A.; Kim, D. H.; Szanyi, J.; Peden, C. H. F. *J. Phys. Chem. C* **2008**, *112* (25), 9486−9492.
(54) Lee, M. H.; Cheng, C.-F.; Heine, V.; Klinowski, J. *Chem. Phys. Lett.* **1997**, *265* (6), 673−676.
(55) Jayaram, V.; Levi, C. G. *Acta Metall.* **1989**, *37* (2), 569−78.
(56) Meephoka, C.; Chaisuk, C.; Samparnpiboon, P.; Praserthdam, P. *Catal. Commun.* **2007**, *9* (4), 546−550.
(57) Macedo, M. I. F.; Bertran, C. A.; Osawa, C. C. *J. Mater. Sci.* **2007**, *42* (8), 2830−2836.
(58) Bruehne, S.; Gottlieb, S.; Assmus, W.; Alig, E.; Schmidt, M. U. *Cryst. Growth Des.* **2008**, *8* (2), 489−493.
(59) Billinge, S. J. L. *J. Solid State Chem.* **2008**, *181* (7), 1695−1700.
(60) Egami, T. *J. Phys. Chem. Solids* **1995**, *56* (10), 1407−1413.
(61) Michel, F. M. E., L.; Antao, S. M.; Lee, P. L.; Chupas, P. J.; Liu, G.; Strongin, D. R.; Schoonen, M. A. A.; Phillips, B. L.; Parise, J. B. *Science* **2007**, *316*, 1726−1729.
(62) Chupas, P. J.; Chapman, K. W.; Jennings, G.; Lee, P. L.; Grey, C. P. *J. Am. Chem. Soc.* **2007**, *129* (45), 13822−13824.
(63) Gateshki, M.; Chen, Q.; Peng, L.-M.; Chupas, P.; Petkov, V. *Z. Kristallogr.* **2007**, *222* (11), 612−616.
(64) Juhas, P.; Cherba, D. M.; Duxbury, P. M.; Punch, W. F.; Billinge, S. J. L. *Nature* **2006**, *440* (7084), 655−658.
(65) Page, K.; Proffen, T.; Terrones, H.; Terrones, M.; Lee, L.; Yang, Y.; Stemmer, S.; Seshadri, R.; Cheetham, A. K. *Chem. Phys. Lett.* **2004**, *393* (4−6), 385−388.
(66) Petkov, V. *Adv. X-Ray Anal.* **2003**, *46*, 31−36.
(67) Paglia, G.; Rohl, A. L.; Buckley, C. E.; Gale, J. D. *Phys. Rev. B: Condens. Matter Mater. Phys.* **2005**, *71* (22), 224115/1−224115/16.
(68) Christoph, G. G.; Corbato, C. E.; Hofmann, D. A.; Tettenhorst, R. T. *Clays Clay Miner.* **1979**, *27* (2), 81−86.
(69) Finger, L. W.; Hazen, R. M. *J. Appl. Phys.* **1978**, *49* (12), 5823−5826.
(70) Zhang, X.; Honkanen, M.; Levaenen, E.; Maentylae, T. *J. Cryst. Growth* **2008**, *310* (15), 3674−3679.
(71) John, C. S.; Alma, N. C. M.; Hays, G. R. *Appl. Catal.* **1983**, *6* (3), 341−346.
(72) Duevel, A.; Romanova, E.; Sharifi, M.; Freude, D.; Wark, M.; Heitjans, P.; Wilkening, M. *J. Phys. Chem. C* **2011**, *115* (46), 22770−22780.
(73) Kwak, J. H.; Hu, J. Z.; Kim, D. H.; Szanyi, J.; Peden, C. H. F. *J. Catal.* **2007**, *251* (1), 189−194.
(74) Sabarinathan, V. R.; Ganapathy, S. *J. Phys. Chem. B* **2010**, *114*, 1775−1781.
(75) Slade, R. C. T.; Southern, J. C.; Thompson, I. M. *J. Mater. Chem.* **1991**, *1* (4), 563−568.
(76) Chen, F. R.; Davis, J. G.; Fripiat, J. J. *J. Catal.* **1992**, *133* (2), 263−278.
(77) Pecharroman, C.; Sobrados, I.; Iglesias, J. E.; Gonzalez-Carreno, T.; Sanz, J. *J. Phys. Chem. B* **1999**, *103* (30), 6160−6170.
(78) Wang, J. A.; Bokhimi, X.; Morales, A.; Novaro, O.; Lopez, T.; Gomez, R. *J. Phys. Chem. B* **1999**, *103* (2), 299−303.
(79) Perander, L. M.; Zujovic, Z. D.; Groutso, T.; Hyland, M. M.; Smith, M. E.; O'Dell, L. A.; Metson, J. B. *Can. J. Chem.* **2007**, *85* (10), 889−897.
(80) Smith, S. J.; Page, K.; Kim, H.; Campbell, B. J.; Boerio-Goates, J.; Woodfield, B. F. *Inorg. Chem.* **2012**, *51* (11), 6421−6424.
(81) Tsuchida, T.; Horigome, K. *Thermochim. Acta* **1995**, *254*, 359−70.
(82) Lindackers, D.; Janzen, C.; Rellinghaus, B.; Wassermann, E. F.; Roth, P. *Nanostruct. Mater.* **1999**, *10* (8), 1247−1270.
(83) Sohlberg, K.; Pennycook, S. J.; Pantelides, S. T. *J. Am. Chem. Soc.* **1999**, *121* (33), 7493−7499.
(84) Sohlberg, K.; Pennycook, S. J.; Pantelides, S. T. *Chem. Eng. Commun.* **2000**, *181*, 107−135.
(85) Wolverton, C.; Hass, K. C. *Phys. Rev. B: Condens. Matter Mater. Phys.* **2001**, *63* (2), 024102/1−024102/16.

(86) Navrotsky, A. *Int. J. Quantum Chem.* **2009**, *109* (12), 2647−2657.

dx.doi.org/10.1021/ic302593f | *Inorg. Chem.* 2013, 52, 4411−4423